Dilated Divergence Based Scale-Space Representation for Curve Analysis

Max W.K. Law[1,2,*], KengYeow Tay[2,3], Andrew Leung[2,3],
Gregory J. Garvin[2,4], and Shuo Li[1,2]

[1] GE Healthcare, Canada
[2] University of Western Ontario, London, Canada
[3] London Health Sciences Centre, London, Canada
[4] St. Joseph's Health Care London, London, Canada
max.w.k.law@gmail.com

Abstract. This study proposes the novel dilated divergence scale-space representation for multidimensional curve-like image structure analysis. In the proposed framework, image structures are modeled as curves with arbitrary thickness. The dilated divergence analyzes the structure boundaries along the curve normal space in a multi-scale fashion. The dilated divergence based detection is formulated so as to 1) sustain the disturbance introduced by neighboring objects, 2) recognize the curve normal and tangent spaces. The latter enables the innovative formulation of structure eccentricity analysis and curve tangent space-based structure motion analysis, which have been scarcely investigated in literature. The proposed method is validated using 2D, 3D and 4D images. The structure principal direction estimation accuracies, structure scale detection accuracies and detection stabilities are quantified and compared against two scale-space approaches, showing a competitive performance of the proposed approach, under the disturbance introduced by image noise and neighboring objects. Moreover, as an application example employing the dilated divergence detection responses, an automated approach is tailored for spinal cord centerline extraction. The proposed method is shown to be versatile to well suit a wide range of applications.

1 Introduction

Scale-space theory [1,2,3,4,5,6,7,8,9] has been actively studied for decades for the recognition and detection of blob-like, curvilinear and planar local image structures. The conventional scale-space detection is performed by invoking a diffusion process for the analysis of an image signal. The duration of the diffusion process implicitly defines the detection scale. In this regard, scale-space approaches are mainly designed to manipulate the diffusion tensor or post-process the resultant image of the diffusion process to perform detection. During the analysis at a particular scale-level, undersized image details and structures are generally suppressed. Nonetheless, the intensity variation in the vicinity of structures is

possibly independent to the structure. For instance, the widths of the separation between bones and the attached soft tissue in medical images are small and do not scale according to the sizes of the adjacent interested objects. These narrow object separations can be annihilated at a coarse detection level for recognizing large objects. In addition, for eccentric curves, such as ellipsoid or elliptical curvilinear structures, the disagreement of object scales along different orientations is unconsidered in the aforementioned conventional scale-space techniques.

In this study, a dilated divergence based scale-space framework is proposed. It is formulated to precisely capture thin edges of large structure and simultaneously avoid the disturbance introduced by other closely positioned objects. The proposed method is designed to handle curves in multi-dimensional images. The curve structures such as spherical, curvilinear, and planar or some volumetric structures can be generally modeled as curves with arbitrary thickness[1]. Along the curve tangent space, intensity changes of the curves are minimal, while abrupt intensity changes are observed across the structure boundary along the curve normal space. The proposed method is devised to capture these abrupt intensity changes. Object scales are estimated according to the responses acquired in various scales. Furthermore, identifying the curve normal and tangent spaces enables the analysis of structure eccentricity to recognize the structure geometry, and the analysis of structure motion based on spatial-temporal curve tangent space.

Distinct to the linear scale-space methods [1,3,6,8,9], the proposed method considers fine image details for recognizing large structures. It is non-diffusion based and hereby utilizes no expensive iterative computation as most of the nonlinear scale-space methods [2,4,5,7] require. At each detection scale, the detection responses are acquired as a set of linear image filtering responses. It well handles the curve eccentricity and is also helpful for low level curve motion estimation. It is beneficial to a wide range of image processing application, such as road (1D curves in 2D images) extraction, intracranial vein or spinal cord (eccentric 1D curves in 3D images) segmentation, and coronary artery or trachea motion (2D curves in 4D images) analysis.

2   Dilated Divergence

The divergence of a vector field $\boldsymbol{f}(\boldsymbol{x})$ is defined as

$$\mathrm{div}(\boldsymbol{f}(\boldsymbol{x})) \equiv |\delta C(\boldsymbol{x})|^{-1} \lim_{C(\boldsymbol{x}) \to 0} \int_{\delta C(\boldsymbol{x})} \boldsymbol{f}(\boldsymbol{x} + \boldsymbol{y}) \cdot \boldsymbol{da}, \qquad (1)$$

where $C(\boldsymbol{x})$ is an infinitesimal region centered at $\boldsymbol{x}$, $\boldsymbol{y}$ is the position vector inside C, $\boldsymbol{da}$ is the outward normal of the region surface and its magnitude is the infinitesimal area on δC. The divergence operator falls into the category of second order derivatives operation. The scale-space methods in this category

---

[1] E.g. blob-like, curvilinear and planar structures are zero-dimensional curves, onedimensional curves and two-dimensional curves respectively.

mainly serve the detection of curve structures based on diffusion based image smoothing, such as curvilinear structure analysis [7,9,10].

The dilated divergence of $\boldsymbol{f}$ is defined as $\mathcal{D}^r(\boldsymbol{f}) = -|\delta S_r|^{-1} \int_{\delta S_r} \boldsymbol{f} \cdot \boldsymbol{da}$, where S_r is a n-ball of radius r and n is the dimensionality of $\boldsymbol{f}$. The sign of the operator is reverted in order that bright structures produce positive responses. For simplicity of discussion, the position vector $\boldsymbol{x}$ is omitted hereafter. Distinct to the diffusion based scale-space approaches, the detection scale of the proposed framework is governed by the detection radius r.

The above dilated divergence is general to process any vector field $\boldsymbol{f}$ in any dimension. In this study, the image gradient is employed to form the dilated divergence descriptor $\mathcal{D}^r(\nabla I)$. Employing the image gradient, this descriptor aims at capturing information about the intensity changes occurring across object boundaries. The descriptor is designed to convey a strong detection response at the center of a curve structure, when the hypersphere radius coincides with the structure semi-thickness. This situation implies that the boundary of the curve structure touches the hypersurface, where the image gradient at the contact positions is aligned with $\boldsymbol{da}$ and S_r is centered at the center of the object. For the hypersurfaces of other concentric hyperspheres associated with different radii, dilated divergence produces low or no responses. It is because undersized hypersphere cannot reach the object boundary while when a hypersurface overshoots the object boundary, $\boldsymbol{da}$ is not parallel to the image gradient that penalizes the response.

2.1   Anisotropic Dilated Divergence

Distinct to 0D curves which yield significant intensity variations along all directions, the higher-dimensional curves exhibit low or no intensity changes in one or more directions. Detection of these structures requires an orientation sensitive descriptor. Given an arbitrary detection direction $\hat{\nu}$, an anisotropic dilated divergence is obtained as $\mathcal{D}^r((\nabla I \cdot \hat{\nu})\hat{\nu})$. On the one hand, a well adjusted detection direction helps selectively capture intensity changes along the curve normal directions. On the other hand, through inspecting the anisotropic dilated divergence responses along various directions, structure orientations are computed. The anisotropy of this descriptor subsequently enables the detection of object scales along different principal directions, thereby yielding the analysis of structure eccentricity. By generalized Stroke's theorem, the anisotropic dilated divergence operator is rewritten as,

$$\mathcal{D}^r((\nabla I \cdot \hat{\nu})\hat{\nu}) = \hat{\nu}^T \left[\frac{1}{|\delta S_r|} \int_{S_r} \mathcal{H}(I)dv \right] \hat{\nu}, \tag{2}$$

where $\mathcal{H}$ is the Hessian matrix of the image. This equation allows the anisotropic dilated divergence responses to be synthesized based on tensor $\frac{1}{|\delta S_r|} \int_{S_r} \mathcal{H}(I)dv$. Denoting this tensor by $\mathcal{T}^r(I)$, it can be computed efficiently by applying the Fourier transform,

$$\mathcal{T}^r(I) = -\frac{4\Gamma(\frac{n+1}{2})}{r^{\frac{n}{2}}\pi^{\frac{n-3}{2}}} \mathcal{F}^{-1}\left(\mathcal{F}(I)||\boldsymbol{\omega}||^{-\frac{n}{2}} \boldsymbol{\omega}\boldsymbol{\omega}^T B_{\frac{n}{2}}(2\pi r||\boldsymbol{\omega}||) \right), \tag{3}$$
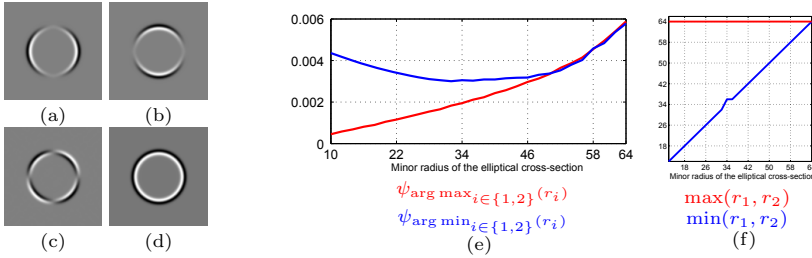
Fig. 1. (a-d) The anisotropic dilated divergence obtained based on a 2-D dirac image function δ, $j = 0$, $r = 16$ and $\sigma = 2$. (a, b) The diagonal elements of $\mathcal{T}^{r,j}$ that are equivalent of the responses of $\mathcal{D}^r((\nabla\delta \cdot \hat{\nu})\hat{\nu})$ where $\hat{\nu}$ is the horizontal direction in (a), and the vertical direction in (b). (c) The image of the off-diagonal elements of $\mathcal{T}^{r,j}(\delta)$. (d) The image of $\text{Tr}(\mathcal{T}^{r,j}(\delta))$, which is equivalent to the sum of the images shown in (a) and (b). (e, f) Different responses obtained at the center of a 1D curve with elliptical cross-section (major radius=64 unit-length) in a 3D image.

where $\mathcal{F}$ and $\mathcal{F}^{-1}$ are respectively the multidimensional Fourier transform and inverse Fourier transform operators, $\boldsymbol{\omega}$ is the frequency domain position vector in cycle-per-unit-length, Γ is the Gamma function and B_k is the kth order Bessel function of the first kind. The tensor based computation allows an analytical form estimation of the most contributive detection direction, i.e.

$$\arg \max_{\hat{\nu}} |\mathcal{D}^r((\nabla I \cdot \hat{\nu})\hat{\nu})| = \arg \max_{\hat{\nu}} |\hat{\nu}^T \mathcal{T}^r(I)\hat{\nu}|.$$

This optimization procedure results in an eigen-decomposition at each local position. In which, the most contributive detection directions are the eigenvectors of $\mathcal{T}^r(I)$ associated with the largest absolute value of the eigenvalues.

2.2   Multi-scale Detection and Scale Selection

For curve analysis, the dilated divergence response is induced from the intersecting space between the hypersuface and object boundaries. In discrete image analysis, the intersection is an n dimensional space. The dilated divergence responses are normalized according to the hypervolume of the intersection. Denote σ is the voxel-length of an image, the image gradient can be regarded as piecewise constant within an interval of σ. From this perspective, the scale normalization is elaborated in Appendix A.

Meanwhile, applying the band-unlimited dilated divergence operator to the band-limited discrete signal causes aliasing artifacts. This is overcome by a Gaussian smoothing with a scale factor equal to σ in the dilated divergence operation. With the Gaussian smoothing and the curve dimensionality based scale normalization, the final anisotropic dilated divergence tensor is calculated as,

$$\mathcal{T}^{r,j} = -\left(\frac{r}{\sqrt{2r\sigma - \sigma^2}}\right)^j \frac{4\Gamma(\frac{n+1}{2})}{r^{\frac{n}{2}}\pi^{\frac{n-3}{2}}} \mathcal{F}^{-1}\left(\mathcal{F}(I)e^{-2\pi\sigma^2||\boldsymbol{\omega}||^2}||\boldsymbol{\omega}||^{-\frac{n}{2}}\boldsymbol{\omega}\boldsymbol{\omega}^T B_{\frac{n}{2}}(2\pi r||\boldsymbol{\omega}||)\right),$$
(4)

where j is the dimensionality of the curve, which is defined beforehand depending on the types of the desired curves. This tensor is symmetric and has $n \times n$ entries which contains $\sum_{i=1}^{n} i$ independent channels. For $n = 2$, Figs. 1a-c illustrate the three independent channels of $\mathcal{T}^{r,j}$ and Fig. 1d exemplifies the trace of $\mathcal{T}^{r,j}$. As multiplication in the frequency domain is equivalent to convolution in the spatial domain, $\mathcal{T}^{r,j}(\delta)$ can be regarded as a group of image filters capturing the intensity changes occurring at the interested scale defined by r. The scale-normalized dilated divergence is capable of performing multi-scale analysis using a set of pre-defined radius set. The maximum radius and radius-interval of the radius set are respectively suggested to be the semi-thickness of the largest target structure in the image, and 0.5σ according to the Nyquist rate. The best detection scale at each local position is chosen by comparing the responses obtained across different scales.

During the scale selection, at each scale, the dilated divergence responses influenced by descending and ascending intensity edges are assessed separately. In the n eigenvalues of $\mathcal{T}^{r,j}$, the positive and negative ones are produced by descending and ascending intensity transitions respectively. Denote the largest-magnitude eigenvalue and its eigenvector at the scale r are γ_1^r and $\hat{\varphi}_1^r$,

$$\lambda_1^r = \max \left\{ \max_{\delta \in \{\sigma, 1.5\sigma, 2\sigma...r\}} \left(\gamma_1^\delta \right), 0 \right\} + \min \left\{ \min_{\delta \in \{\sigma, 1.5\sigma, 2\sigma...r\}} \left(\gamma_1^\delta \right), 0 \right\}. \quad (5)$$

This measure is formulated using the competition between the largest ascending intensity change and the descending counterparts. It penalizes the responses obtained from oversized scales, of which the detection hyperspheres overshoot the object boundary and reach adjacent one exhibiting opposite intensity changes. The optimal detection scale is selected based on the strongest detection responses obtained over multiple scales up to the maximum detectable scale to be $\mathbf{R}$,

$$r_1 = \min \left(\arg \max_{r \in \{1.5\sigma, 2\sigma, 2.5\sigma...\mathbf{R}\}} |\lambda_1^r| \right), \psi_1 = \lambda_1^{r_1}, \hat{e}_1 = \hat{\varphi}_1^{r_1}. \quad (6)$$

The scale selection omits the smallest scale σ because at which the competition is always disabled. This selection procedure searches for a scale where the response magnitude first attains its maxima. It gives strongest responses at object centers, while the signs of the detection responses are reverted across the object boundaries analogous to other second derivatives based approaches.

2.3   Eccentricity Analysis and Structure Orientation

The curves which exhibit a 2 or higher dimensional normal space can possess eccentric intensity patterns (e.g. 2D ellipse and tubular structures with elliptical cross-sections) and yield different object scales along various directions. In eccentricity analysis, the procedures to extract detection responses, the optimal detection orientation and scale selection are reiterated at all principal directions of the curve normal space to capture the possibly disagreed object scales along

different direction. Given the analysis of the first $m-1$ basis of the normal space is completed, the mth basis is acquired by performing eigen-decomposition on,

$$(Q_m)^T T^{r,j} Q_m, \tag{7}$$

where $Q_m = \text{IDTY} - \sum_{i=1}^{m-1} \hat{e}_i(\hat{e}_i)^T$, and IDTY is an identity matrix. This produces at most $n - m$ non-zeros eigenvalues. Denote the largest-magnitude eigenvalue and the corresponding eigenvector are γ_m^r and $\hat{\varphi}_m^r$ respectively, the response at scale r is obtained based on the competition between the descending and ascending intensity transition responses, analogous to Eq. 5,

$$\lambda_m^r = \max \left\{ \max_{\delta \in \{\sigma, 1.5\sigma, 2\sigma \ldots r\}} \left(\gamma_m^\delta \right), 0 \right\} + \min \left\{ \min_{\delta \in \{\sigma, 1.5\sigma, 2\sigma \ldots r\}} \left(\gamma_m^\delta \right), 0 \right\}. \tag{8}$$

Saddle points on the intensity surface at which the detection responses possess different signs are not the focus of this study. The scale selection of eccentricity analysis prefers the responses showing the same response sign as ψ_1. The desired scale level r_m, response ψ_m and basis $\hat{e}_m$ are,

$$r_m = \min \left(\arg \max_{r \in \{1.5\sigma, 2\sigma, 2.5\sigma \ldots \mathbf{R}\}} \left(sign(\psi_1) \lambda_m^r \right) \right), \psi_m = \lambda_m^{r_m}, \hat{e}_m = \hat{\varphi}_m^{r_m}. \tag{9}$$

An example of the responses and scales delivered by this eccentricity analysis is given in Figs. 1e and f. Finally, the curve tangent space is the orientations along which the object possesses minimal intensity variation. The orthogonal basis of the curve tangent space is the non-singular eigenvectors of $\text{IDTY} - \sum_{i=1}^{n-j} \hat{e}_i(\hat{e}_i)^T$.

2.4   Spatial-temporal Curve Based Spatial Curve Motion Estimation

Structure motions can be assessed based on image sequences. In an nD image sequence, a moving jD curve yields a $(j + 1)$D curve in the $(n + 1)$D spatial-temporal image. This interpretation allows an intuitive estimation of the low level curve motion without prior segmentation of the structures. The low level curve motion assumes that the curve structure center translation across adjacent time frame is small compared to the semi-thickness of the curve. As such, the structure motion fields are piecewise linear inside the structure and the geometry of a local segment of the curve is unaltered across adjacent time frames. This suits the tracking of deformation induced curve movement, such as extracting the motion of the aorta in image sequences [11].

To formulate the spatial-temporal curve detection, the spatial-temporal voxel length along the time dimension is suggested to be less than or equal to 2σ. Define a $(n + 1)$-by-n matrix $\mathbf{C}$ of which the first n rows form an identity matrix and the $(n + 1)$th row is zero, and let $\hat{u}_1, \hat{u}_2, ..., \hat{u}_j$ the curve tangent space orthogonal basis. In the spatial-temporal image, the $(j + 1)$D curve tangent space basis are $\mathbf{C}\hat{u}_1, \mathbf{C}\hat{u}_2, ..., \mathbf{C}\hat{u}_j$ and an additional basis denoted as $\hat{\tau}$. Given the piecewise

linear assumption, after the time elapsed by Δt, the curve tangent space basis can be expressed as $\hat{u}_i + \Delta t \frac{1}{\hat{\tau} \cdot \hat{T}} \left(\mathbf{C}^T \hat{\tau} \right)$ and thus, the spatial curve motion is,

$$\frac{1}{\hat{\tau} \cdot \hat{T}} \mathbf{C}^T \hat{\tau}. \tag{10}$$

3   Evaluation and Discussion

The proposed method is evaluated based on various criteria in three synthetic and one clinical experiments. The synthetic experiments employ 2D, 3D and 4D images respectively, followed by spinal cord centerline extraction experiment which involves 15 clinical image volumes. In the synthetic images, the interested objects have an intensity value 1 and the background intensity is zero. The images are Gaussian-smoothed with a scale factor of 1 unit-length prior to analysis. The proposed method is compared against two approaches, multi-dimensional $\gamma-$Normalized Hessian method [3,9] and the three-dimensional optimally oriented flux method [12], referred to as HESSIAN and OOF respectively hereafter. These methods, including the proposed method are stemmed from second order techniques. Nonetheless, distinct from the proposed method, HESSIAN omits image details during the analysis of sizable structures, while OOF is developed only for non-eccentric curves embedded in 3D images. The image features extracted from HESSIAN and OOF resemble those from the proposed method in three aspects: they are low level detection approaches that convey general-purpose features for possible subsequent application-specific analysis; they provide scalar "curveness" detection responses and corresponding principal directions; and they are grounded on multi-scale analysis. The scale sets used by the optimally oriented flux and the proposed method are identical, from 1 unit-length to 20 unit-length, with a 0.5 unit-length interval. They both employ a pre-Gaussian smoothing with a 1 unit length scale factor (i.e. $\sigma = 1$ unit-length for the proposed method). The scale set used by the Hessian method contains the same number of scales and dynamic range, but with a fixed geometric step.

3.1   Multi-scale Detection and Scale Selection

The first experiment concerns a single-layer spiral (Fig. 2a). The semi-width of this structure gradually increases from 9 unit-length at the inner end to 10.125 unit-length at the outer end. Two sections of this structure are closely located and their boundaries are in a distance of 1.5 unit-length apart. Fig. 2b demonstrates the response computed from this structure. The anisotropic dilated divergence produces positive responses inside the structure and forms a ridge at the structure centerline. It returns negative responses in the vicinity of the structure. The response pattern inside the structure at the optimal scale is consistent regardless of the curve width change and the disturbance the adjacent segment. In Figs. 2c and d, the response profiles along two different positions of the structure are visualized. Inside the structure, the response ridges show a bifurcation-like
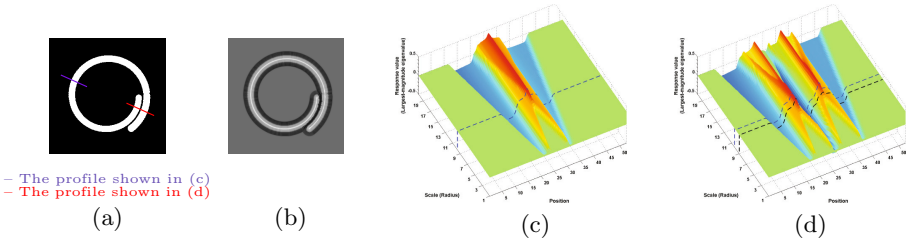
Fig. 2. A 1D curve in a 2D image with a unit pixel size. (a) The original image. (b) The detection response image ψ_1. (c, d) The intermediate multi-scale responses λ_1^r obtained at the highlighted positions shown in (a). The dotted lines illustrate the selected scales based on Eq. 6 which coincide with the ground-truth scale (object semi-width).
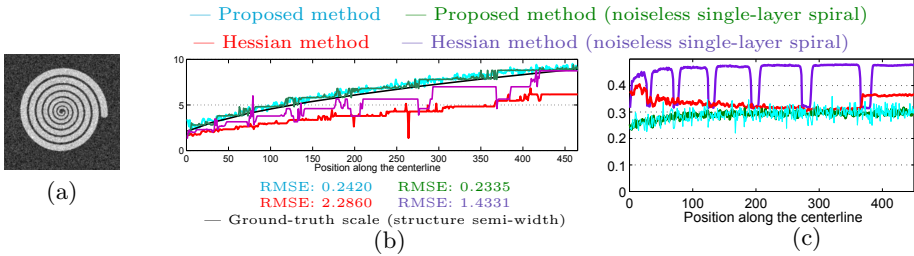

Fig. 3. An experiment of a noise corrupted spiral (1D curve) in a 2D image with a unit pixel size. The radius of the spiral gradually increases from 2 to 10 unit-length. (a) The Gaussian noise (0.2 standard deviation) corrupted spiral. (b) The estimated scales based on the proposed method and the Hessian method. (c) The detection responses based on the proposed method and the Hessian method.

pattern over various scales. The response ridge pair at undersized scales is induced from the boundaries at two opposite sides of the structure. The ridge pair intersects at the structure center when the scale coincides to the structure semi-width and yield a sharp response peak. In Fig. 2c, the response peak sustains in the oversized scales when no neighboring object interfere the detection. When a neighboring object presents, the responses reported at oversized scales are attenuated as evidenced in Fig. 2d. These attenuated responses are consequently eliminated in the scale selection procedures (Eqs. 6 and 9).

Furthermore, a comparison between the proposed method and HESSIAN concerning the multi-scale detection performance is conducted. It involves two set of images - the noise corrupted spiral image (Fig. 3a) and seven noiseless single-layer spiral images. The noiseless single-layer spirals are acquired by partitioning the noiseless spiral into seven single-layer spirals. The study is performed along the spiral centerline in the noisy spiral image and the corresponding single-layer spiral images. Each single-layer spiral is further revolved outward by an angular distance of $\frac{\pi}{8}$ radian (see Fig. 2a for the outermost single-layer spiral). The extended portions of the spirals serve as neighboring objects which possibly interfere the detection. These two sets of images offer three distinct testing

conditions - noisy and with neighboring objects, noiseless and without neighboring objects, and noiseless and with neighboring objects. For HESSIAN, the largest-magnitude eigenvalue is used as the response at each scale and the final responses are chosen according to the maximum magnitude responses over scales. The resultant scales of HESSIAN shows large discrepancies to the ground-truth in various cases (compare the purple and red curves against the black curve, and see the corresponding root-mean-square errors (RMSEs) in Fig. 3b). In the noiseless single-layer spiral tests (the purple curve in Fig. 3b), HESSIAN underestimates structure scales at the beginning of each layer. It is because the further revolved portion of the spiral interferes the detection. These underestimated scales resemble the scales estimated from the noisy spiral (see the overlaps between the red curve and the lower envelop of the purple curve in Fig. 3b).

On the contrary, the scales estimated by the proposed method are accurate (see the largely overlapped cyan, teal and black curves and the small RMSEs in Fig. 3b) regardless of the presence of image noise and closely located objects. This figure illustrates that the proposed method exhibits superior performance over the Hessian method for scale estimation when neighboring objects exist. Similar observation is found in the detection response values shown in Fig. 3c. The proposed method delivers consistent and similar detection responses among the noisy spiral and the noiseless single-layer spiral cases. When neighboring object does not exist, HESSIAN gives a consistent responses despite of the scale changes (see the upper envelop of the purple curve in Fig. 3c), analogous to the proposed method. The response values of both methods are slightly reduced at the thinnest part of the spiral because of the high structure curvature. Nonetheless, when neighboring objects exist, HESSIAN responses drop significantly (the red curve and the lower envelop of the purple curve in Fig. 3c).

3.2   Eccentricity Analysis and Structure Orientation

The eccentricity analysis experiment focuses on the accuracies of estimating object principal axes and the object scales along the axes. It employs a noise corrupted 3D spiral with elliptical cross-section (Figs. 4a and b). The proposed method is compared against HESSIAN and OOF. This image has an anisotropic voxel size that commonly exists in practical 3D image scans. Sinc interpolation [9] is applied for HESSIAN and OOF method to produce isotropic voxels. The responses of these methods at each scale level are the arithmetic mean of the two largest magnitude eigenvalues [9,12]. Their optimal scales are chosen as the maximum magnitude response over scales. At the optimal scales, the structure orientations, major and minor axes are acquired as the eigenvectors associated with the smallest, medium and largest magnitude eigenvalues respectively.

Along the centerline of the spiral, there are three local orientations - the structure orientation, the major and minor axes. In addition, two object scales - major and minor radii are involved. In Fig. 4c, the accuracies of the estimated orientations of various axes based on different methods are shown. In all cases, the proposed method yields significantly lower discrepancies to the ground-truth than HESSIAN and OOF do. Theoretically, the eigenvalue ratios
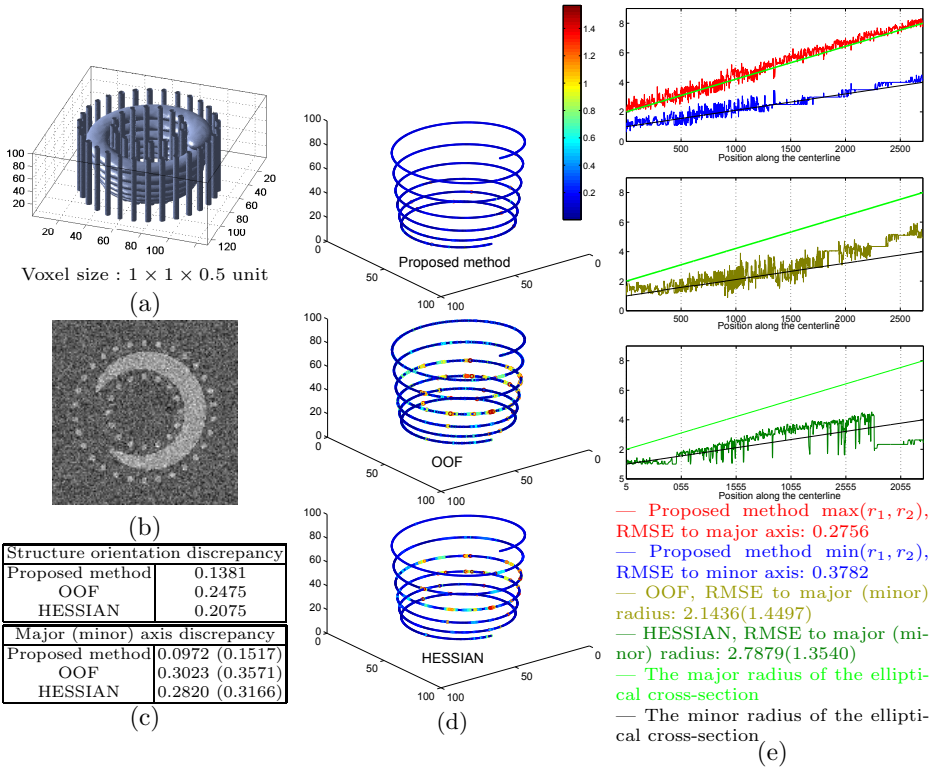
Fig. 4. The experiment on an anisotropic voxel-sized volume. The spiral major and minor radii are 2 and 1 unit-length at the bottom and gradually increase to 8 and 4 at the top. The separation between layers is 1 unit-length. (a) The isosurface of the spiral and its neighboring objects. (b) The $z = 70$ slice of the image volume corrupted by additive Gaussian noise with a 0.3 standard deviation. (c) The mean acute angular discrepancies (in radian) of different local axes measured along the centerline. (d) The acute angular discrepancies (in radian) of the structure orientation estimated along the centerline. (e) The optimal scales extracted by different methods.

of HESSIAN hint the structure eccentricity [13]. However, the disturbance introduced by neighboring objects prohibits the eigenvalues from being extracted at the desired scale. In addition, the circular cross-section assumption imposed by OOF deviates from the elliptical cross-section of this spiral. Their estimation of the structure orientation, the major and minor axes are therefore less accurate. Fig. 4d depicts the profiles of the angular discrepancies of structure orientation estimation based on different approaches. The large discrepancy cases of HESSIAN and OOF are observed in the entire spiral. It suggests that the estimation error is independent to object scales. In Fig. 4e, the estimated object scales for the spiral cross-section are presented. The scales estimated by HESSIAN and OOF fluctuate in between the major and minor radii. In contrast, the proposed method precisely estimates both minor and major radii and shows promising accuracies with RMSEs less than one scale step (0.5 unit-length).

3.3   Spatial-temporal Curve Based Spatial Curve Motion Estimation

In this experiment, a randomly deformed spiral (Fig. 5a) is used for studying the accuracy of the structure centerline motion estimated by the spatial-temporal curve analysis (Eq. 10). During the experiment, Frame-1 and Frame-7 are replicated twice and padded to the volumetric sequence to handle the wrap-around effect of the frequency domain based computation of Eq. 7. Based on Eq. 10, the centerline motion of the Frames-$2, 3, 4, 5, 6$ are retrieved. The motion vector in the Frame-t is employed to predict the centerline position based on the given position in the Frame-$(t - 1)$. Denote q, Δq, $\boldsymbol{c}(q)$, $\boldsymbol{m}(q)$ are time, time interval between adjacent frames, ground-truth centerline positions and the estimated motions at $\boldsymbol{c}(q)$. The predicted positions at the time $q + \Delta q$ are given as $\boldsymbol{c}(q - \Delta q) + 2\Delta q \boldsymbol{m}(q)$. The Euclidean distances (error) between the predicted positions and the ground-truth positions are visualized in Fig. 5b. To help assess the prediction results, Euclidean distances of the ground-truth centerline movement is shown. Towards the end of the sequence, more cases of high curvature positions appear and reduce the accuracy of the estimated curve motion.
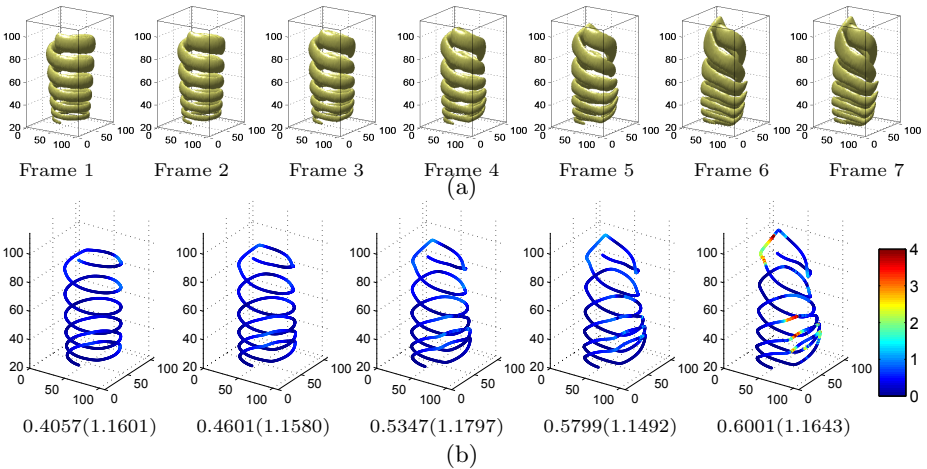

Frame 1   Frame 2   Frame 3   Frame 4   Frame 5   Frame 6   Frame 7
(a)

0.4057(1.1601)   0.4601(1.1580)   0.5347(1.1797)   0.5799(1.1492)   0.6001(1.1643)
(b)

Fig. 5. Motion analysis experiment based on a Gaussian noise (with a 0.2 standard deviation) corrupted, randomly deformed 3D spiral. The major and minor radii are 2 and 1 unit-length at the bottom of the spiral and gradually increase to 8 and 4 at the top of the spiral. The spatial-temporal voxel size is $0.5 \times 0.5 \times 1 \times 2$ unit. (a) The isosurface of the deforming spiral in different time frames. In Frames-$3, 5$ and 7, the spiral is deformed by randomly (according to the uniform distribution) offsetting 64 control points in a range of $[-0.15\times\text{image-length}, 0.15\times\text{image-length}]$ along each dimension. These control point positions are linearly interpolated for Frames-$2, 4$ and 6. Voxel intensity is determined by using bicubic interpolation. (b) The discrepancies between the estimated position and the true position of the spiral centerlines, numbers are shown as "Average centerline displacement compared to the ground-truth".

3.4   Application Example

In the final experiment, 15 volumetric T2-weighted magnetic resonance images (T2-MRI) from the cervical and thoracic spinal regions are employed (Fig. 6). In T2-MRIs, the cord is comprised of a grey center (grey matter) and a dark border (white matter). The spinal cord is surrounded by a bright layer (cerebro-spinal fluid), which exhibits varying thickness, and voxel intensity significantly drops and fluctuates outside this layer. In addition, the intensity contrast across the spinal cord boundary declines towards the bottom slice of an image due to dispersal of the low intensity white matter. Thus, the intensity pattern of the spinal cord is inconsistent, thereby leading to disturbance for spinal cord analysis. As such, spinal cord analysis is extremely challenging.

In our dataset, the spinal cords are approximately vertically aligned 1D eccentric curves (elliptical curvilinear structures) which traverse every slice of the volumetric images, having minor and major radii ranged from 6 to 15 unit-length. In this experiment, the dilated divergence measures ψ_1 and ψ_2 are aggregated as $-\min(\psi_1, 0) - \min(\psi_2, 0)$ to contribute a speed field for shortest-path extraction [14]. The multi-scale selection results based on the sum of the two largest-magnitude eigenvalues of HESSIAN [9] and OOF [12] are employed as
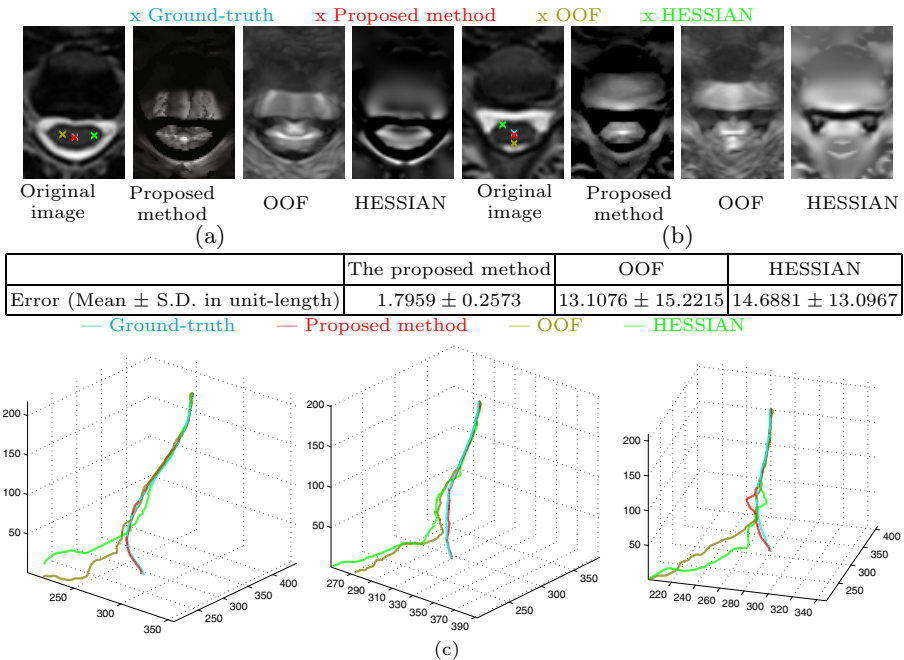

	The proposed method	OOF	HESSIAN
Error (Mean ± S.D. in unit-length)	1.7959 ± 0.2573	13.1076 ± 15.2215	14.6881 ± 13.0967

Fig. 6. Five centerline extraction examples. (a, b) Axial views of regions-of-interest of two cases, the original images and the speed fields computed by different methods. (c) The quantitative centerline extraction result, and three examples of extracted centerlines based on different methods. Errors are measured as the average distance between extracted centerline point samples and the closest ground-truth centerline points.

the speed field for centerline extraction comparison. Subsequent to the construction of the speed fields, two additional slices filled with an infinity speed value are padded beyond the top and bottom slices of the speed fields. The shortest-path source and destination are positioned at the corners of these two slices respectively, constituting a fully automatic spinal cord centerline extraction algorithm. This experiment concerns two aspects, handling eccentric curves surrounded by structure possessing inconsistent intensity pattern; and finding the path corresponding to the target curve in a large volumetric image ($512 \times 512 \times 200$ voxels, voxelsize $1 \times 1 \times 2.1157$ unit, 1 unit-length $= 0.4727$mm in this experiment), i.e. reporting distinguishable and strong responses inside the curves as compared to those inside irrelevant structures. Spinal cord-specific knowledge is excluded from the formulation of the speed fields of all methods. Therefore, the experimental results generally reflect the performance of the examined methods on handling different eccentric curves.

In Figs. 6a and b, the proposed method gives strong detection responses at the centerline of the spinal cord, while OOF and HESSIAN supply strong responses close to the boundary of the cord and lead to incorrect extraction. The significant HESSIAN response difference between the cases shown in Figs. 6a and b suggests that HESSIAN is extremely sensitive to the intensity fluctuation outside the curve. Meanwhile, OOF is solely developed for circular curvilinear 1D curve. It reports strong responses in multiple positions on the curve cross-section (Figs. 6a and b, OOF) and results in erroneous centerline extraction. In addition, the largely overlapped cyan and red lines and crosses in Figs. 6a-c illustrate the accurate centerlines extracted by the proposed method. On the contrary, OOF and HESSIAN result in large disagreements in the extraction result. Furthermore, the extracted centerlines of OOF and HESSIAN are driven away from the spinal cords towards the tracking source points located at the origin. It manifests that OOF and HESSIAN cannot supply distinguishable responses inside curve structures. Finally, the centerline extraction errors shown in Fig. 6c further evidences the very accurate and stable centerline extraction based on the proposed method, compared to those based on OOF and HESSIAN.

4   Conclusion

This paper proposes the novel dilated divergence based scale-space representation for curve analysis. The proposed scale-space framework is non-diffusion based. Its computation is grounded on linear filters and therefore, it is efficient and parallelizable. The proposed method is studied and validated in three aspects - scale selection, eccentricity analysis and spatial-temporal curve analysis. In particular, the dilated divergence addresses analysis of structure eccentricity and spatial-temporal curve tangent space which have been scarcely studied.

In the experiments, the proposed method is shown to be capable of sustaining the disturbance introduced by closely positioned objects. It outperforms conventional scale-space approaches in the comparison. The formulation of the proposed framework is general to serve a wide range of applications. Investigation of the

dilated divergence framework for detection of saddle points on intensity surface for corner and junction recognition, structure centerline extraction, 0D curve based-salient feature detection, curve segmentation and curve motion tracking, particularly for high dimensional curves are the future direction of this research.

References

1. Mikolajczyk, K., Schmidt, C.: Scale & affine invariant interest point detectors. IJCV 60, 63–86 (2004)
2. Weickert, J.: A review of nonlinear diffusion filtering. In: Scale-Space, pp. 3–28 (1997)
3. Lindeberg, T.: Edge detection and ridge detection with automatic scale selection. IJCV 30, 117–156 (1998)
4. Perona, P., Malik, J.: Scale-space and edge detection using anisotropic diffusion. PAMI 12, 629–639 (1990)
5. Okada, K., Comaniciu, D., Krishnan, A.: Scale selection for anisotropic scale-space: application to volumetric tumor characterization. In: CVPR, vol. 1, pp. 594–601 (2004)
6. Lowe, D.: Distinctive image features from scale-invariant keypoints. IJCV 60, 91–110 (2004)
7. Manniesing, R., Viergever, M., Niessen, W.: Vessel enhancing diffusion a scale space representation of vessel structures. MedIA 10, 815–825 (2006)
8. Deng, H., Zhang, W., Mortensen, E., Dietterich, T., Shapiro, L.: Principal curvature-based region detector for object recognition. In: CVPR, pp. 1–8 (2007)
9. Sato, Y., Nakajima, S., Shiraga, N., Atsumi, H., Yoshida, S., Koller, T., Gerig, G., Kikinis, R.: Three-dimensional multi-scale line filter for segmentation and visualization of curvilinear structures in medical images. MedIA 2, 143–168 (1998)
10. Krissian, K.: Flux-based anisotropic diffusion applied to enhancement of 3-D angiogram. TMI 21, 1440–1442 (2002)
11. Biesdorf, A., Wörz, S., Müller, T., Weber, T.F., Heye, T., Hosch, W., von Tengg-Kobligk, H., Rohr, K.: Model-Based Segmentation and Motion Analysis of the Thoracic Aorta from 4D ECG-Gated CTA Images. In: Fichtinger, G., Martel, A., Peters, T. (eds.) MICCAI 2011, Part I. LNCS, vol. 6891, pp. 589–596. Springer, Heidelberg (2011)
12. Law, M.W.K., Chung, A.C.S.: Three Dimensional Curvilinear Structure Detection Using Optimally Oriented Flux. In: Forsyth, D., Torr, P., Zisserman, A. (eds.) ECCV 2008, Part IV. LNCS, vol. 5305, pp. 368–382. Springer, Heidelberg (2008)
13. Frangi, A.F., Niessen, W.J., Vincken, K.L., Viergever, M.A.: Multiscale Vessel Enhancement Filtering. In: Wells, W.M., Colchester, A.C.F., Delp, S.L. (eds.) MICCAI 1998. LNCS, vol. 1496, pp. 130–137. Springer, Heidelberg (1998)
14. Sethian, J., Vladimirsky, A.: Fast methods for the eikonal and related hamilton-jacobi equations on unstructured meshes. PNAS 97, 5699–5703 (2000)

A   Appendix - Scale Normalization

Given a 1D curve in a 2D image where $\boldsymbol{\nu}$ is the curve 1D-normal space, σ is the edge diffuseness, which is analyzed by a circular region (S_r in Eq. 2) represented as $y = \sqrt{R^2 - x^2}$, $\sigma < R$ and image gradient has a unit magnitude within the edge and is null anywhere else, the anisotropic dilated divergence response is,

$$\frac{1}{\pi R} \int_{R-\sigma}^{R} \frac{x}{R} \int_{-\sqrt{R^2-x^2}}^{\sqrt{R^2-x^2}} dy dx = \frac{2}{\pi R} \sqrt{2R\sigma - \sigma^2}.$$

An appropriate normalization is $\frac{\pi R}{2}\sqrt{2R\sigma - \sigma^2}$. Without loss of generality, define an nD image patch $J(\boldsymbol{x})$, which consists of a jD curve centered at the local position $\boldsymbol{x}$. Denote $\hat{u}_1, ..., \hat{u}_j$ and $\hat{u}_{j+1}, ..., \hat{u}_n$ are the orthogonal basis of the curve normal space and the curve tangent space respectively. Eq. 2, the dilated divergence for J can be re-written as, $\hat{\nu}^T \left[\frac{1}{|\delta S_r|} \int_{S_r} \mathcal{H}(J) \left(\int_{S_r} d\hat{u}_1...d\hat{u}_j \right) dj \hat{+} 1_1...d\hat{u}_n \right] \hat{\nu}$. The inner integral is independent to the image term (analogous to $\int_{-\sqrt{R^2-x^2}}^{\sqrt{R^2-x^2}} dy$ in the above 2D image example). The nested integrals along the tangent space become a multiplicative factor to the outer integrals operated along the normal space. As such, given $\hat{\nu}$ is one of the principal directions in the curve normal space and r equals to the structure semi-thickness along $\hat{\nu}$,

$$\mathcal{D}^r((\nabla I \cdot \hat{\nu})\hat{\nu}) \propto \left(\frac{r}{\sqrt{2r\sigma - \sigma^2}} \right)^j. \tag{11}$$